

# LOCALIZED AMBIENT NOISE TOMOGRAPHY OVER THE FORGE UTAH SITE

---

by Andy J. Trow<sup>1</sup>, Kristine L. Pankow<sup>1</sup>, Yadong Wang<sup>2</sup>, and Fan-Chi Lin<sup>2</sup>

<sup>1</sup>University of Utah Seismograph Stations, University of Utah, Salt Lake City, Utah

<sup>2</sup>Department of Geology and Geophysics, University of Utah, Salt Lake City, Utah



**Miscellaneous Publication 169-J**

**Utah Geological Survey**

*a division of*

UTAH DEPARTMENT OF NATURAL RESOURCES

This paper is part of *Geothermal Characteristics of the Roosevelt Hot Springs System and Adjacent FORGE EGS Site, Milford, Utah*. <https://doi.org/10.34191/MP-169>

Bibliographic citation:

Trow, A.J., Pankow, K.L., Wang, Y., and Lin, F.-C., 2019, Localized ambient noise tomography over the FORGE Utah site, *in* Allis, R., and Moore, J.N., editors, *Geothermal characteristics of the Roosevelt Hot Springs system and adjacent FORGE EGS site, Milford, Utah*: Utah Geological Survey Miscellaneous Publication 169-J, 15 p., <https://doi.org/10.34191/MP-169-J>.



# LOCALIZED AMBIENT NOISE TOMOGRAPHY OVER THE FORGE UTAH SITE

by Andy J. Trow, Kristine L. Pankow, Yadong Wang, and Fan-Chi Lin

## ABSTRACT

In December 2016 and August 2017 two geophone arrays recorded 30 days of seismic data near Milford, Utah, to perform ambient noise tomography, centered on the Frontier Observatory for Research in Geothermal Energy (FORGE) Utah project site. The initial deployment in December 2016 consisted of 93 5-Hz three-component geophones roughly centered on the FORGE project area but spanning across the Mineral Mountains and into the Milford Valley. The second deployment in August 2017 consisted of 49 densely spaced geophones centered about the FORGE deep test well site. Ambient noise cross-correlations were calculated using 10-minute windows for all station pairs. The individual correlation functions were then stacked in order to estimate the Green's functions for virtual source and receiver paths. For the initial 93-station deployment, clear Rayleigh wave signals were observed in the 3 to 10 second period range. During the August 2017 dense deployment, signals were observed between 0.5 and 1 seconds. Frequency-time analysis was used to obtain surface wave dispersion measurements from the cross-correlation functions for both arrays. Dispersion measurements were inverted for Rayleigh wave group velocity maps at 3, 5, and 7 second periods for the initial 93-station array. Sensitivity kernels indicate that these periods are sensitive to depths from 2.5 to 8 km. Group velocity maps show a general trend of higher velocities in the core of the Mineral Mountains with lower velocities in the alluvium of the Milford Valley. For the 3 to 7 second periods, group velocities range from 2 to 3.5 km/s, but show the top of a low-velocity layer beginning to develop at 5 to 8 km depth. This low-velocity zone is consistent with work from a previous teleseismic tomography study. For the dense array, a group velocity map was determined for the 0.67-second period, which roughly correlates to the upper 500 m. This map shows higher velocities (600 m/s) at the eastern portion of the array, closer to the Mineral Mountains consistent with the shallowing of a granitic reservoir unit and thinner alluvial cover.

## INTRODUCTION

As part of site characterization efforts for the Utah Frontier Observatory for Research in Geothermal Energy (FORGE) project, two geophone seismic monitoring arrays were deployed over the FORGE project area in order to record both microseismicity and ambient noise for seismic imaging (Trow et al., 2018). The instruments are compact 5-Hz three-component Nodal geophones. Other studies using this instrumentation have proven its applicability to earthquake detection and crustal imaging studies (Bowden et al., 2015; Li et al., 2015, 2018; Hansen and Schmandt, 2015; Wang et al., 2017). Specifically, these geophone arrays facilitate high-resolution crustal imaging at periods below 10 seconds (e.g., Wang et al., 2017; Ward and Lin, 2017; Wu et al., 2017). For imaging we use ambient noise cross-correlation records to estimate the Green's function between a virtual source station and receiver (Shapiro and Campillo, 2004). Primarily, we extracted Rayleigh wave signals from the vertical-vertical noise cross-correlations.

The study area is located in southwestern Utah to the northeast of Milford, Utah, on the western flank of the Mineral Mountains (Figure 1). This area has undergone many investigations to understand its geothermal potential since the late 1970's (e.g., Ward et al., 1978; Robinson and Iyer, 1981), and geologic and thermal conditions have been summarized in more recent reports (Hardwick et al., 2016; Simmons et al., 2016; Allis et al., 2017). Overall, the region is characterized by high heat flow and Quaternary volcanism (Blackwell, 1983; Edwards and Chapman, 2013) with crystalline basement rock (Moore and Nielson, 1994). The high heat flow can be attributed to thinning crust in the Basin and Range Province along with an active volcanic history (e.g., Benz et al., 1990). Recent volcanism began in the Oligocene (Faulder, 1991) with emplacement of the granitic rocks beginning about 25 Ma, with the most recent rhyolite flows and domes occurring about 0.5 to 0.8 Ma (Robinson and Iyer, 1982; Faulder, 1991).

Structural interpretations (Smith and Bruhn, 1984; Barker, 1986) of seismic profiles across the project site, extending from the Mineral Mountains into the Milford Valley, highlight a major reflector dipping westward into the basin that could be a low-angle listric fault or a basement rock-sediment contact. In addition, teleseismic P-wave tomography indicates a low-velocity zone beneath the western portion of the Mineral Mountains (Robinson and Iyer, 1981). This zone has been identified in the upper crust below the study area at depths between 5 and 15 km (Robinson and Iyer, 1982; Barker, 1986) with up to a 7% reduced P wave seismic velocity indicating higher basement temperatures and the possibility of partial melt. Low-velocity

anomalies and areas of elevated crustal temperatures are important for understanding the heat source of the Roosevelt Hot Spring System. We propose the use of ambient noise seismic tomography to look for and better constrain these along with other structures in the FORGE project area.

To map seismic velocities, continuous seismic data is used to perform noise cross-correlations between geophone stations. This allows an estimation of the Green's functions along the path between station pairs (Shapiro et al., 2005; Yao et al., 2008). Surface wave tomography is performed on a grid by inverting travel-time measurements (Barmin et al., 2001; Lin et al., 2008, 2013; Ward, 2015). This technique has been applied to the high-permeability zone in a geothermal reservoir in portions of Europe (Calò et al., 2013; Lehujeur et al., 2017) and has identified low-velocity regions in known geothermal fields that have been interpreted to be geothermal reservoirs (Calò et al., 2013). Repeated experiments that show mapped velocity changes can relate to changes in the reservoir of the geothermal system. Group velocity measurements from this study will serve as a base model to establish reservoir changes as the geothermal field evolves with development and production during the Utah FORGE project (Simmons et al., 2018).

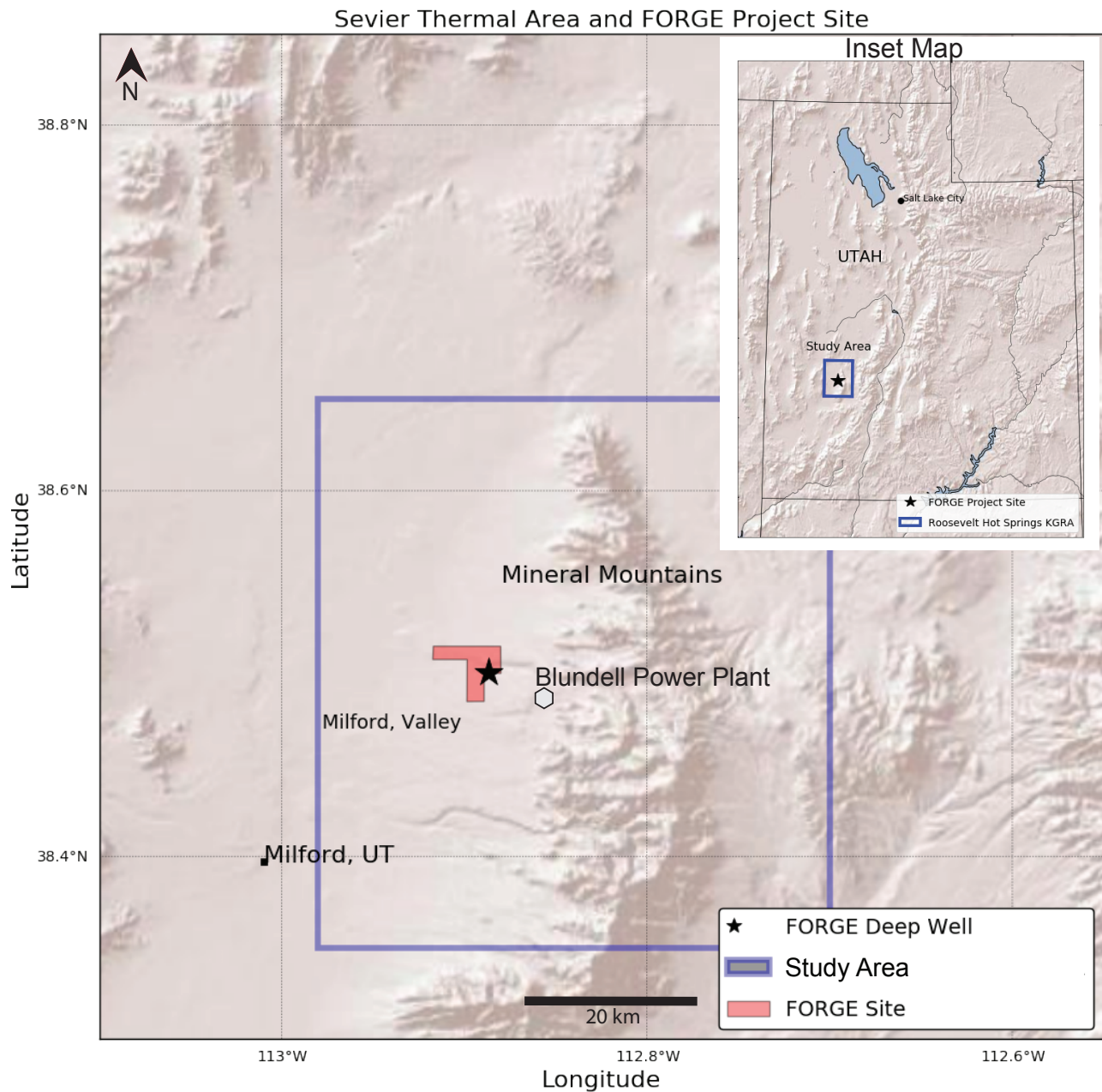


**Figure 1.** Overview Map of Utah FORGE project area and Roosevelt Known Geothermal Resource Area (KGRA). Inset map shows the Roosevelt KGRA (blue box) and FORGE site within the state of Utah. The detailed map shows the footprint of the proposed research facility, the deep well location, and location of the Blundell geothermal power plant.

## DATA

Two seismic deployments were conducted in December 2016 and August 2017 (Figure 2) (Trow et al., 2018). Each experiment lasted ~30 days and consisted of 93 and 49 5-Hz three-component Nodal geophones, respectively. Array geometry was designed to maximize its aperture while maintaining equal station spacing in order to optimize crossing source-receiver ray paths. Recorded seismic waveforms were sampled at 250 Hz with a pre-amp gain of 18 dB. Deployments generated ~250 to 500 GB of time series data. Figure 1 shows the study area, Figure 2 gives the detailed array geometry.

The 2016 deployment included 44 geophones spaced at ~4 km, and a central dense grid of 49 geophones with 650 m station spacing. The dense portion of the array was centered over the proposed Utah FORGE geothermal research facility footprint (Figure 1) and the sparse grid covered the Milford Valley and spanned across the Mineral Mountains for seismic event detection and imaging. The full 93-station array (December 2016) was used to extract longer period surface waves that will sample deeper in the crust but will have lower lateral resolution.

During the 2017 deployment the central dense portion of the FORGE array (49 stations) was re-occupied during drilling of the test well. The dense grid has 650 m spacing, which enabled short-period surface waves to propagate between station pairs and show clear move-out in the cross-correlation functions (CCF). Surface wave records between 0.5 and 1 seconds were extracted allowing higher lateral resolution, and imaging of shallower structure due to near-surface sensitivity of the surface waves at these frequencies.

## NOISE SOURCE ANALYSIS

Ambient noise seismic tomography is sensitive to azimuthal variations and frequency content of the noise source. Reliability of travel-time measurements is affected by source characteristics, which are important inputs of tomographic inversion problems (Snieder, 2004). Wang et al. (2017) show minor changes to tomographic inversion results at Mount St. Helens after imposing a correction to an azimuthally biased noise source distribution. Since inhomogeneous noise plays a minor role in final results, it is not corrected for in this study. The continuity of the frequency of persistent noise sources is another consideration, such that, depth resolution can be hampered due to restricted sensitivity from a limited bandwidth of noise sources. Data from the arrays showed promising move-out in two discrete ranges: 3 to 10 seconds and 0.5 to 1 seconds. The 2016 deployment of 93 stations showed coherent signal in the 3 to 10 second range. We do not consider signal

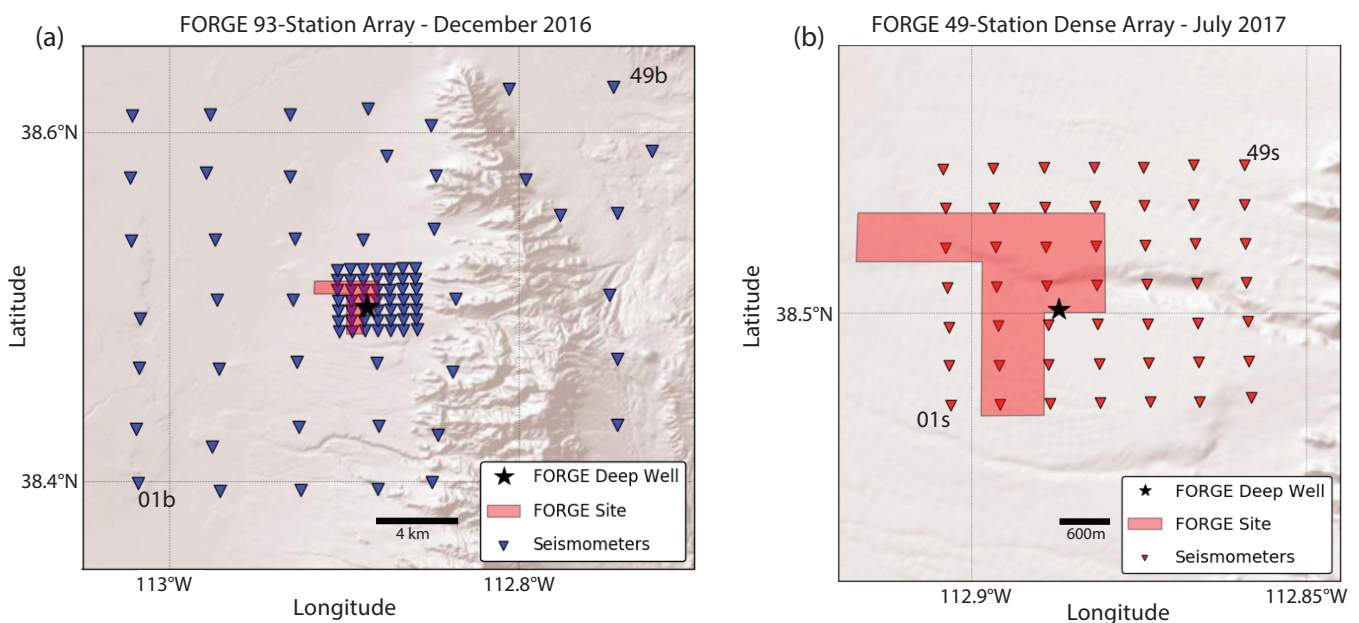


**Figure 2.** Detailed array map of the two deployments. (a) The full 93-station deployment from December 2016. Outer grid has about 4 km spacing with a dense grid of 49 stations spaced at 650 m. (b) August 2017 re-occupation of 49-station dense grid. Close up of the 650-m-spaced dense array. Both maps have the footprint of the FORGE facility in red and the deep well location.

beyond 10-second periods due to the limited aperture of the array ( $\sim 30$  km). The 3 to 10 second signal corresponds with the secondary oceanic microseismic peak ( $\sim 8$  sec) (Haubrich et al., 1963). At shorter periods the signal was strongly influenced by a near vertically arriving signal that did not propagate across the array as a surface wave. Body wave energy is strongest between 1 and 3 seconds and causes challenges for imaging 1 to 3 km depths.

The 2017 49-station dense array was re-occupied to measure small drilling-related seismic events and record ambient noise records during the summer. During re-occupation of the dense grid, we see a homogeneous signal between 0.5 and 1 seconds that was used to measure group velocity. Move-out was clear on positive and negative lags of record sections indicating a homogenous source. We compared the dense grid stations for both FORGE deployments to assess the higher frequency signal variation during different seasons as well as local variation in noise source distribution (Figure 3). The record section shows the cross-correlations from the furthest southwest station 01s as the virtual source to all other receivers. The re-occupied dense grid has a higher signal-to-noise ratio (SNR) and a more homogeneous noise distribution (Figure 3a), while the dense portion of the initial array deployed in December has weaker signals and stronger move-out only in the negative lags of the CCFs (Figure 3b).

## METHODS

For crustal imaging we use ambient noise cross-correlation to establish Rayleigh wave group velocity structure beneath the array. This tomography process has been well documented by Bensen et al. (2007) and we follow the procedure described in Lin et al. (2013) to calculate the cross-correlations. This process is completed in three steps: (1) Prepare data for each station including spectral whitening, followed by calculation of the noise cross-correlation records from continuous seismic data and temporal normalization of each cross-correlation record. (2) Measure Rayleigh wave group travel-times through frequency-time analysis (FTAN) (Levishin et al., 1989; Bensen et al., 2007). (3) Invert travel-time measurements on a 2D grid (Barmin et al., 2001) to obtain smooth group velocity maps of the region for the periods where we see strong Rayleigh wave signals in the CCFs.

### Data Preparation and Cross-Correlation

The aperture of the initial FORGE deployment in December 2016 consisting of 93 stations is approximately 30 km. The aperture of the re-occupied 49-station dense grid is approximately 6 km. Both experiments had a one-month duration, and we follow the same processing steps for each dataset. Time series data are cut into 10-minute segments for each array. Each segment is spectrally whitened based on the average of the horizontal components, and then for every station pair, we calculate

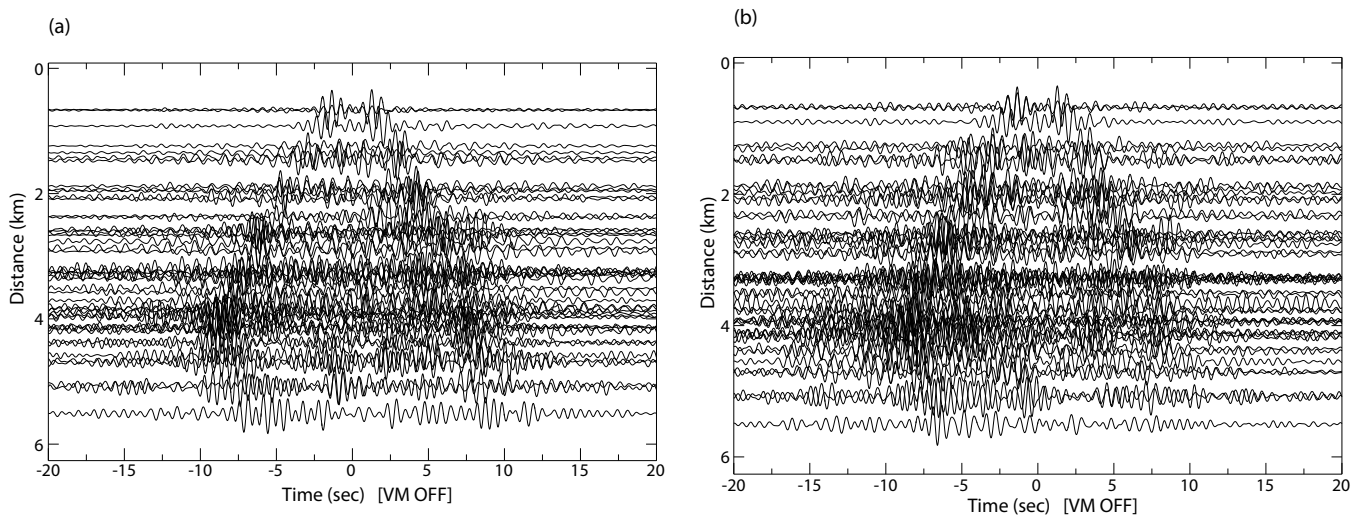


**Figure 3.** Temporal variance in shorter period (0.5–1 second) signal illustrated by plotting the record sections of the CCF's bandpass filtered between 0.5 and 1 second for the dense portion of the FORGE array. (a) Record section for the July 2017 deployment when only the dense portion of the grid was occupied. Signal is more symmetric and has a higher SNR. This illustrates a more homogeneous and stronger noise source during this deployment. (b) Record section for only the dense portion of the grid for the December 2016 FORGE deployment. The signal is stronger on the negative lags of the CCF's and has azimuthal bias in the noise source distribution.

the cross-correlation functions for each 10-minute time window. Resulting cross-correlation results are normalized in the time domain by running-absolute-mean normalization (Bensen et al., 2007). We stack the 10-minute-long window normalized CCF's to obtain a final interstation CCF, which approximates the Green's function between stations (Lin et al., 2013). The processing steps effectively remove transient earthquake signals and other large-amplitude signals including spurious noise spikes (Bensen et al., 2007; Lin et al., 2013).

We compute the cross-correlation for all nine components (EE, EN, EZ, NN, NE, NZ, ZE, ZN, ZZ). The horizontal component cross-correlation functions are rotated into radial and transverse components in order to isolate Rayleigh and Love wave energy and determine which components have the highest SNR. Figure 4 shows a comparison of rotated components of the CCF between station 01b and station 49b. It is clear that the vertical-vertical (ZZ) component result has the highest SNR. For this reason, we focus efforts on the ZZ component results. Using the ZZ component ensures that we extract predominantly Rayleigh wave energy.

The number of cross-correlations computed scales by a factor of  $n^2/2$  where  $n$  is the number of stations. For the full FORGE array, over 4000 cross-correlations are calculated using the 93-station grid and 1,200 are calculated for the re-occupied dense array. Stacked CCFs can be evaluated for positive and negative time lag. Figure 5 is a record section of non-symmetric CCFs for the full FORGE array that is bandpass filtered from 4 to 7 seconds. The asymmetry in the records is due to a non-homogeneous azimuthal distribution of noise. At these longer periods we determine that the main surface wave energy directionality has a southwesterly back-azimuth. To improve SNR on the negative lag of the CCF, the positive and negative lags are averaged to produce a symmetric CCF.

### Group Velocity Extraction

Group velocities are measured through frequency-time analysis (FTAN) over the ZZ component CCF's. FTAN has been used to estimate velocities of the fundamental mode Rayleigh wave (e.g., Levishin et al., 1989; Bensen et al., 2007). We use the automated process outlined in Bensen et al. (2007) and Lin et al. (2008) where each CCF is subject to a series of narrow band-pass filters each having a unique center frequency. After applying a Hilbert transform to the cross-correlation time series, the real portion is combined with the imaginary portion to obtain an envelope function. The max amplitude or peak of the envelope function is picked and corresponds to a time lag ( $t$ ). This time lag is used with the interstation distance ( $d$ ) and time ( $t$ ) to compute the group velocity ( $V_g$ ) via:

$$V_g = \frac{d}{t}$$

where  $V_g$  denotes group velocity,  $d$  is distance, and  $t$  is time (full details are given in Lin et al. (2008)).

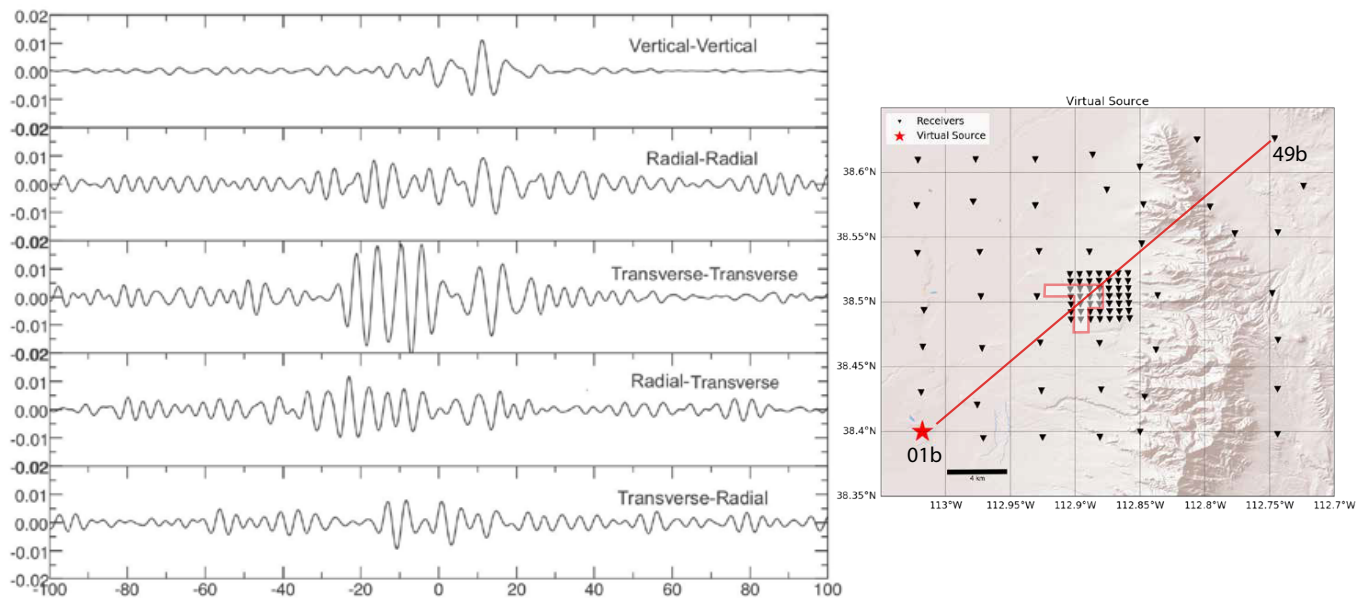


**Figure 4.** Cross-correlation functions for station 01b-49b. The traces are bandpass filtered from 3 to 10 seconds and components are listed for each CCF. We note that the vertical-vertical component has the highest SNR. The strong signal on the vertical-vertical component shows that the signal is dominated by Rayleigh wave energy.

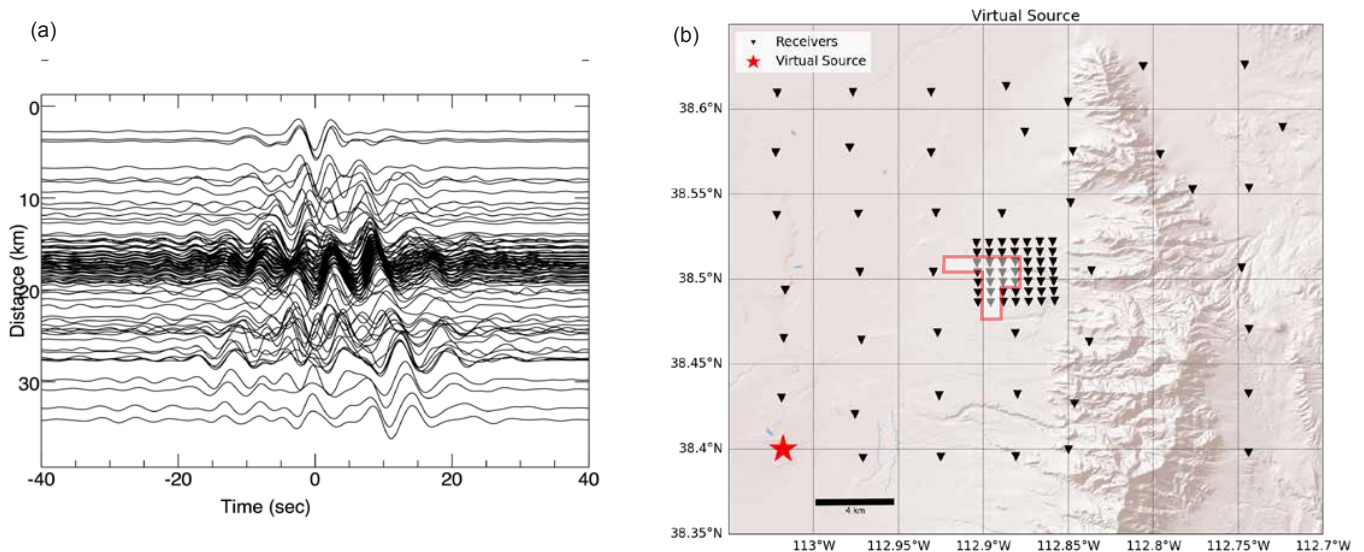


**Figure 5.** Record section of FORGE cross-correlation functions (CCF). (a) The CCF's bandpass filtered from 4 to 7 seconds. Each trace is a one-month stack of 10-minute windows. (b) Map highlighting the virtual source (01b) and receiver map used to plot record section.

To ensure reliable measurements we imposed a minimum distance criterium and a SNR criterium for every station pair. It has been shown that more reliable velocity measurements are obtained when the minimum distance between virtual source and receiver station is three wavelengths (Bensen et al., 2007), but more recent studies have produced robust phase velocity maps using only one wavelength as a minimum distance criterium (Wang et al., 2017). Our group velocity measurements may have bias due to the one wavelength as a minimum distance criterium but with the interstation spacing and limited period band where signal was clear, we were restricted to this shorter criterium. The dense geophone arrays in this study are best suited for a minimum distance criterium of one wavelength, rather than two or three wavelengths (Lin et al. 2008, 2013) because the array apertures are relatively small, and a shorter minimum distance criterium maximizes the number of crossing ray paths, which is a key element to generating robust velocity maps. For 3-second period signals we estimate an average velocity of 2 km/s, and a corresponding minimum distance of  $\sim 6$  km. For the dense array we evaluate a 1-second period wave where we estimate an average velocity of 400 m/s, related to unconsolidated basin sediment, and therefore, we have a minimum distance of roughly 400 m. Additionally we require a SNR criterium of 4, which is measured after the FTAN pick window as defined by estimated crustal velocities and interstation distances. SNR is calculated as the maximum amplitude in the FTAN pick window divided by the root-mean-squared amplitude in the CCF following the FTAN pick window. Once travel-time measurements have passed the quality control criteria, they are stored in a matrix corresponding to each station pair in the array.

### Tomographic Inversion

We use the fundamental-mode Rayleigh-wave group velocity measurements to produce tomographic velocity maps for 3, 5, and 7 second periods for the full 93-instrument grid and a 0.67 second map for the dense 49-station grid. We follow the surface wave inversion method outlined in Barmin et al. (2001) that performs a regularized inversion in two dimensions. We divide our model into an evenly spaced grid ( $0.001^\circ \times 0.001^\circ$ ). The inversion process minimizes the misfit of the travel-time residuals for all ray paths. Regularization includes both smoothing and damping of the function. The regularization is determined empirically, and a suite of inversion parameters are tested to obtain the best parameterization. A tradeoff curve showing the model misfit with smoothing parameters is plotted in Figure 6. The smoothing consists of a weighted smoothing parameter alpha ( $\alpha$ ), and a spatial smoothing parameter sigma ( $\sigma$ ). Optimum smoothing parameters are determined when model residuals are minimized (Figure 6) and results do not contain sharp artifacts. A suite of parameters are tested while keeping the others fixed. We do not use damping, as ray path coverage is regular and well distributed. We look to reproduce smooth features consistent with geologic models when establishing the best model. We note that main high-velocity features remained consistent throughout testing of different parameters. We combine inversion results from the dense central grid at higher frequencies with longer period results from the whole array to improve resolution in the center of the array. Figure 7 shows ray path coverage for both arrays. High ray path density yields an overdetermined inverse problem. The number of ray paths decline as the period increases; this is due to the minimum distance and SNR criteria that are imposed after velocity measurements are made.

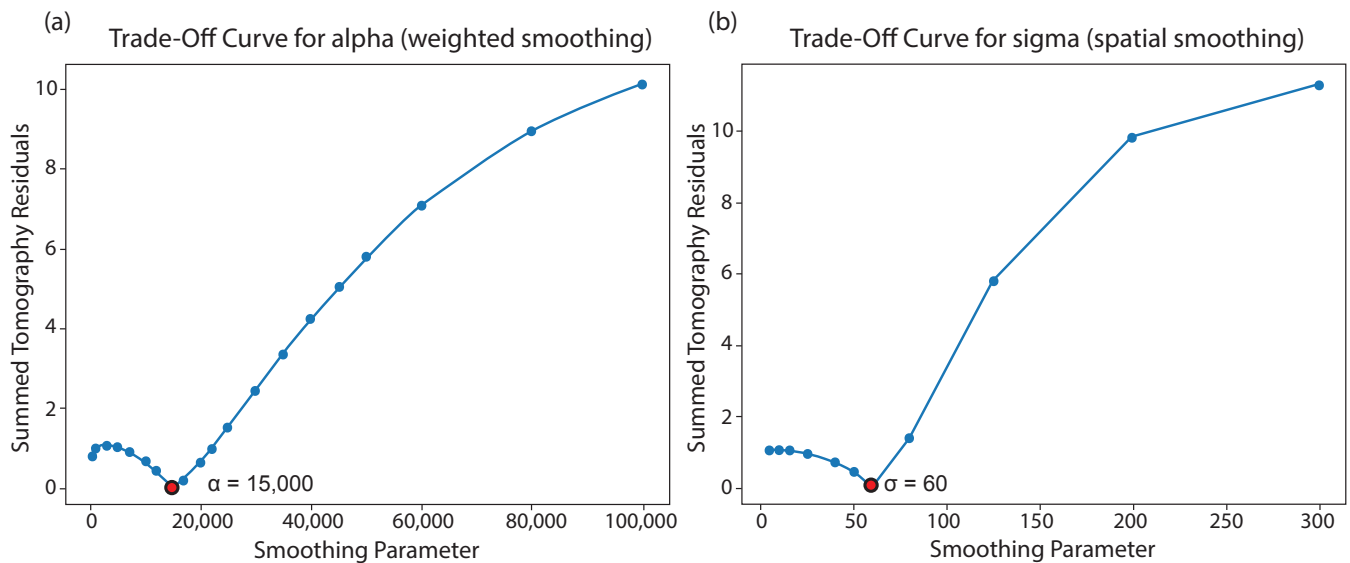


**Figure 6.** Trade-off curves used in determining smoothing parameters during inversion process. Optimum smoothing was determined empirically and parameters were chosen when the inversion residuals are minimized. **(a)** Relationship between weighted smoothing parameters and the inversion residuals. **(b)** Relationship between the spatial smoothing parameters and inversion residuals. A red marker indicates the selected smoothing values.

### Depth Sensitivity Kernels

To better estimate the depth of the resulting velocity maps we calculate two-dimensional depth sensitivity kernels for the fundamental mode Rayleigh-wave group velocities at 3, 5, and 7 second periods (Figure 8a). This is done using a western U.S. (WUS) velocity model that was developed by Herrmann et al. (2011) and adopted for the Utah region in Whidden and Pankow (2012) (Figure 8b). Sensitivity kernels are calculated by calculation of the partial derivative of the predicted surface wave velocity with respect to shear wave velocity as outlined in Wang et al. (2017). Figure 8a shows that the inversion process produces maps that are most sensitive around 3 km depth for 3 seconds, 5 km depth for 5 seconds, and 7.5 km depth for 7 seconds. Sensitivity for the 0.67 period map was in the upper 500 m of the crust.

## RESULTS

We performed cross-correlations between each possible source receiver pair. Move-out of the surface waves is observed in the record sections for both arrays but at different dominant periods; Figure 9 shows a record section for the 49-station dense array and Figure 5a is a record section for the full 93-station array. The signal is most clear and strongest in the 3 to 10 second period band for the entire FORGE array while on the dense array we see it most clear between 0.5 and 1 seconds. The record sections of the symmetric component CCF's show approximate group velocities of 2.3 km/s at 7 second period and 0.5 km/s at 0.67 second period. Based on the ray-path coverage maps, the models are well constrained at the location of the dense grid for both arrays with decreasing resolution towards the edges of the array. Velocity measurements in general are the most well constrained where there is a high density of crossing ray paths.

Figure 10 shows the results from the tomographic inversion. We inverted for group velocities at 0.67, 1, 3, 5, and 7 seconds, respectively. Note that as period increases, group velocities become most sensitive to increasingly deeper velocity structures.

Results from the broad 93-station array show, in general, higher velocities near and below the Mineral Mountains with lower velocities at the edges of the arrays where the basin-fill sediments are deeper and more prominent. However, areas of lower seismic velocities also tend to occur near the edges of the array where velocity measurements are not as well constrained. Figure 10a shows the 7 second Rayleigh wave group velocity map, where we see a prominent high-velocity anomaly (>3 km/s) coincident with the Mineral Mountains to the east of the dense grid. If we trace the outline of the mountain range from satellite imagery we see that the velocity anomaly correlates in space with the granitic Mineral Mountains (Figure 10).

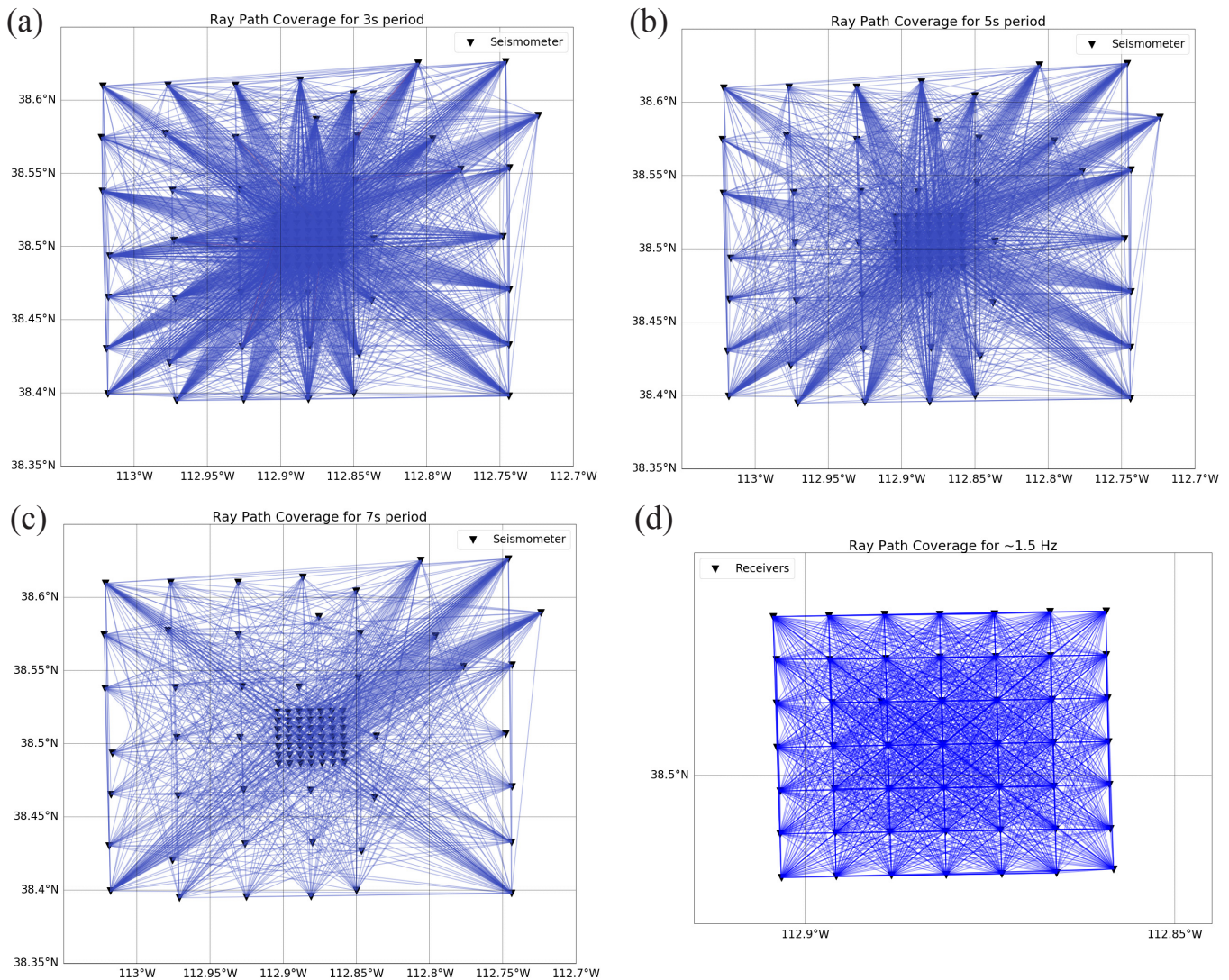


**Figure 7.** Ray path coverage of main FORGE grid. Great circle paths are plotted between virtual source and receiver pairs showing approximate surface wave ray path. Note decreasing ray density as period increases; this is due to minimum distance criteria of one wavelength between virtual source and receiver. (a) 3 second period, (b) 5 second period, (c) 7 second period, (d) 0.67 second period map of dense 49-station grid deployed in July 2017.

## DISCUSSION

The tomographic method reproduces major geologic features in the region. In general, the Mineral Mountains are imaged as a high-velocity anomaly ( $>3$  km/s) and the basins towards the edges of the arrays are relatively slower. Our results indicate as the period of the surface waves increase, and investigation depth increases, there is a reduction in group velocity values. Typically, seismic velocity increases with depth, but beneath the central portion of the Mineral Mountains it reverses. A typical model would show increasing group velocity with depth; however, ours begins to highlight decreasing velocities at roughly 8-km depth. We have plotted the velocity maps with a constant velocity scale (Figure 11) to illustrate this change rather than relative changes due to structure. The decrease in seismic velocity between 5 and 8 km depth corresponds spatially with the high-attenuation body outlined in Robinson and Iyer (1981) where a low-velocity, and highly attenuative body was identified at 5 to 15 km depth using teleseismic tomography. This low-velocity zone could have implications for the heat source of the geothermal basin and is likely related to recent magmatism and volcanism in the region. Depth sensitivity in our analysis is limited to 8 km so we cannot estimate the lower boundary of this low-velocity zone. It is also difficult to estimate the lateral extent of the low-velocity zone, because of poor ray coverage at the longer periods.

In the shorter period range (0.5–1 seconds), we measure seismic velocities of 400 to 500 m/s and we interpret this to be basin-fill sediment. At 0.67 seconds we estimate we are imaging the upper 500 m of the subsurface. The 400 m/s seismic velocities

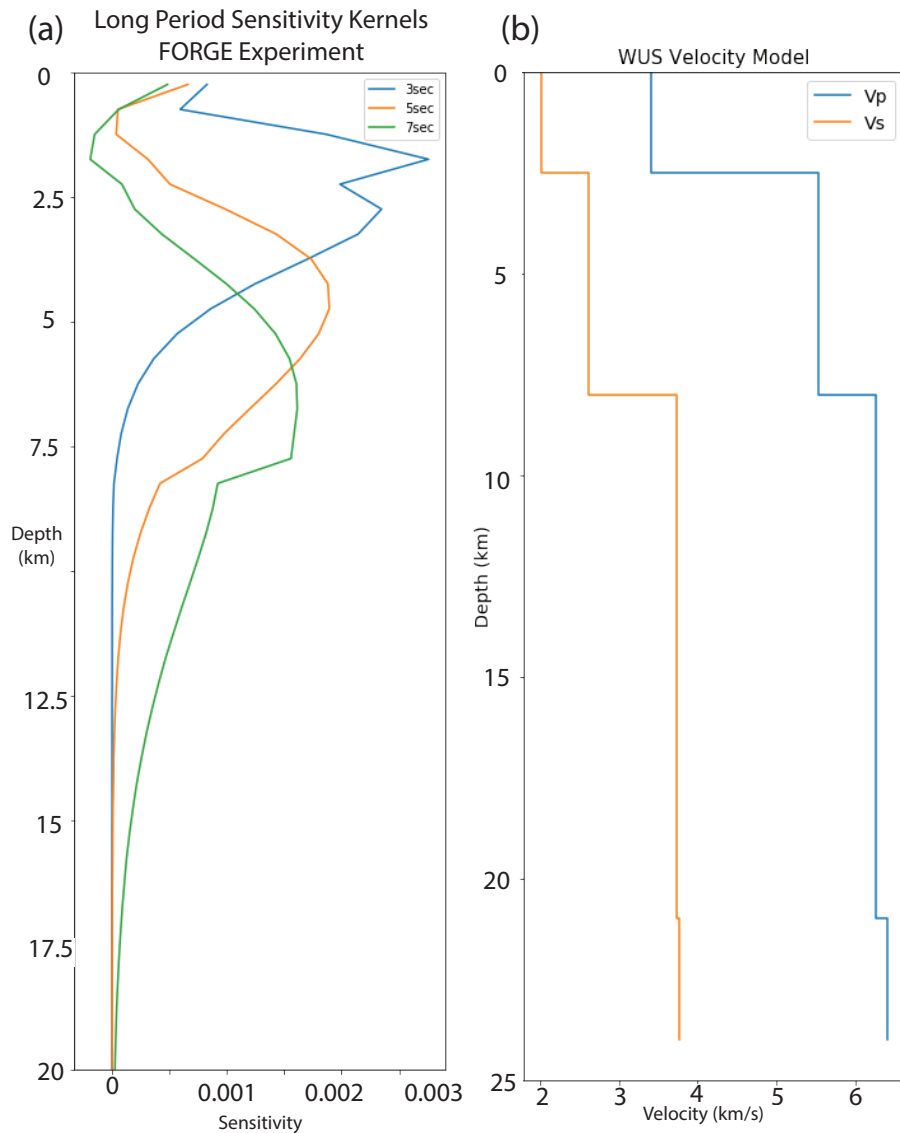


**Figure 8. (a)** Sensitivity kernels for 3, 5, and 7 second period surface waves. We note that depth sensitivity for tomographic models is in the upper 10 km of crust with sensitivity near 2.5 km, 5 km, and 7.5 km, respectively. Western U.S. (WUS) velocity model (Hermann et al., 2011; Whidden and Pankow, 2012) was used in computation of sensitivity kernels and is plotted in (b).

are consistent with results from Spatial Autocorrelation (SPAC) VS30 results in the same region (Zhang and Pankow, 2018). The trend towards higher velocity in the eastern portion of the array, closer to the Mineral Mountains, reflects a shallowing of the alluvium-bedrock contact. This structure is consistent with a strong shallow to moderately dipping reflector identified by Smith and Bruhn (1984).

If looking at absolute group velocities rather than relative changes, there is a decrease of group velocity as period increases. There is a low-velocity zone beneath the western edge of the Mineral Mountains identified by Robinson and Iyer (1981) that has been mapped to similar depths as seen in the 7-second group velocity map.

When considering the dense 49-station grid, we see a general trend of higher velocities to the east, and slower velocities moving basinward to the west (Figure 10b). The dip of the basement rock-sediment interface in this region may affect group velocity measurements at short periods. As the contact becomes shallower towards the east, it is likely that our measurements are increasingly more sensitive to basement rocks. The short-period velocities (0.67 s, 400–500 m/s) are roughly five times slower when compared to measurements at the longer periods.

The tomographic method does not account for topographic changes. While the peaks of the Mineral Mountains are close to 900 m higher than the valley, the great circle distance between two stations on either side of the Mineral Mountains changes by a fraction of a percent between a path along surface topography versus a path assuming a spherical earth. Because inverted

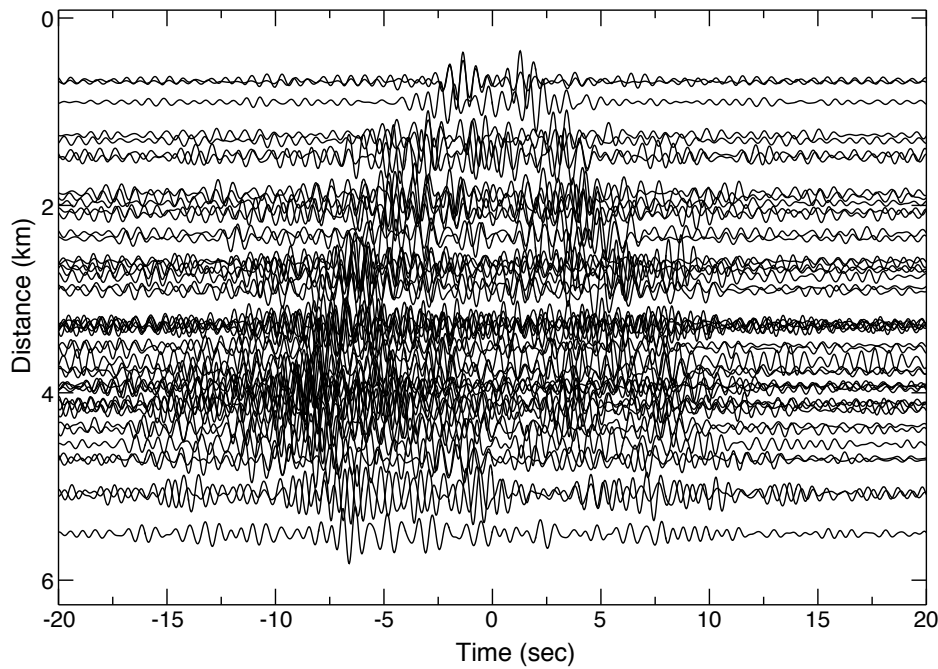


**Figure 9.** Record section of FORGE dense array (49 stations) cross-correlation functions (CCF) bandpass filtered from 0.5 to 1 second. Each trace is the one-month stack of 10-minute windows. Virtual source (01s) is station in southwest corner of the dense array (Figure 5b) that is cross-correlated with all other stations in the dense array.

surface wave group velocity measurements vary by up to 20%, we can assume the majority of travel-time residuals are due to seismic velocity changes, rather than differences in path length from the assumed spherical path that ignores topography used in this study. Previous work on volcanoes in the Pacific Northwest has shown there is very little travel-time bias due to topographic effects (Wang et al., 2017) when major geologic features are the contributing factor to travel-time anomalies.

Finally, our model results are not well constrained. We have limited periods where velocity measurements are made. This is due to noise sources recorded by the FORGE array that are limited between 3 to 10 seconds (full deployment) and 0.5 to 1 seconds (dense deployment). This gives us little depth sensitivity and therefore a full 3D model was not constructed.

## CONCLUSION

Shallow crustal imaging has been performed within the Milford Valley at the FORGE Utah site using dense geophone arrays. One-month deployments generate sufficient ambient seismic noise records to estimate the Green's functions in the upper crust. Cross-correlations were calculated using data collected during the December 2016 93-station full deployment at surface wave periods between 3 and 10 seconds. ZZ component cross-correlations were used to determine fundamental mode Rayleigh wave velocities. These records were used to measure group velocities at 3, 5, and 7 second periods. The dense grid of 49 stations was re-occupied July 2017 during a drilling phase of the FORGE project and was used to extract higher frequency surface waves between 0.5 and 1 seconds. Dispersion measurements were obtained through automated frequency-time analysis of the stacked cross-correlation results and were inverted to produce smooth velocity maps over the FORGE project site. The velocity maps indicate regions of high seismic velocities in the central Mineral Mountains and slower velocities towards the edges of the arrays where basin fill is deeper. For the longer period inversion results, velocities in the Mineral Mountains reach 3.2 km/s whereas the slower basin velocities are  $\sim 2$  km/s. This is due to sediment cover affecting the surface wave group velocity. The sediment cover is thinner or non-existent in the core of the mountains and therefore the surface waves are sampling bedrock, but when moving away from the mountains alluvial deposits are thicker and have slower surface wave velocities than pure bedrock. Shear wave velocities have not been calculated in this study but could be calculated using the sensitivity kernels and could be compared to the well logs of the FORGE well. A low-velocity zone exists below 5 km depth and is coincident with a high-attenuation, low-velocity zone identified by Robinson and Iyer (1981). This low-velocity zone could be related to the heat source of the geothermal system beneath the FORGE footprint. At higher frequency, we measure increasing velocities in the east portion of the dense array with seismic velocities of 400 to 600 m/s. The depth of investigation is estimated at the upper 500 m of the subsurface. This 400 m/s measurement is

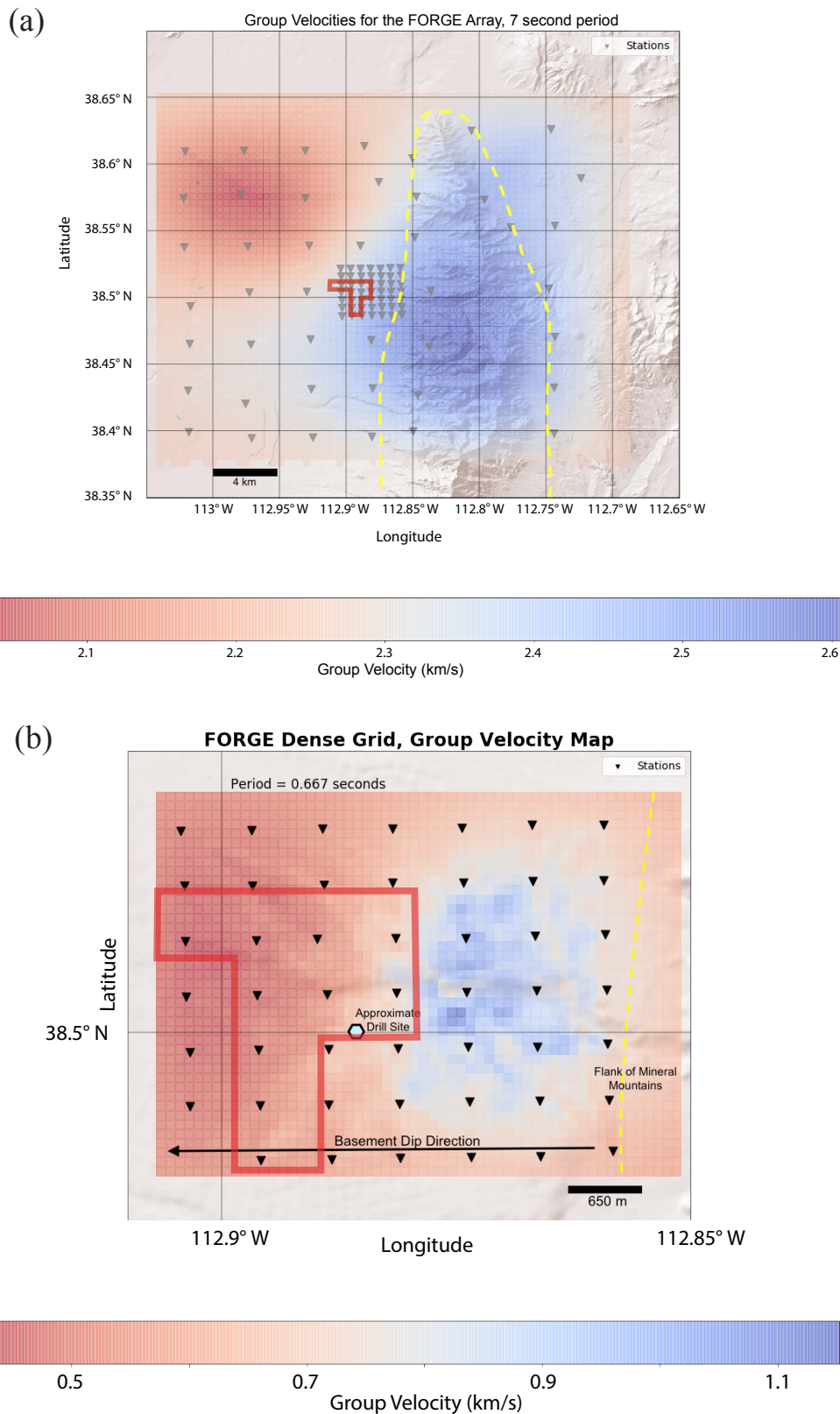


**Figure 10.** (a) Tomographic model obtained using 7 second period data from 93-station array. The majority of the Mineral Mountains high-velocity anomaly remains consistent at different periods. Dashed yellow line outlines approximate boundaries of granitic basement outcropping in the Mineral Mountains. Smoothing here is based on values selected by plotting tradeoff curves (Figure 6), but we note that main high-velocity features are consistent through multiple sets of smoothing parameters. (b) Inversion results from dense 49-station array. Boundary of Mineral Mountains is outlined in yellow. Basement sediment contact dips to west. FORGE site is highlighted in red.

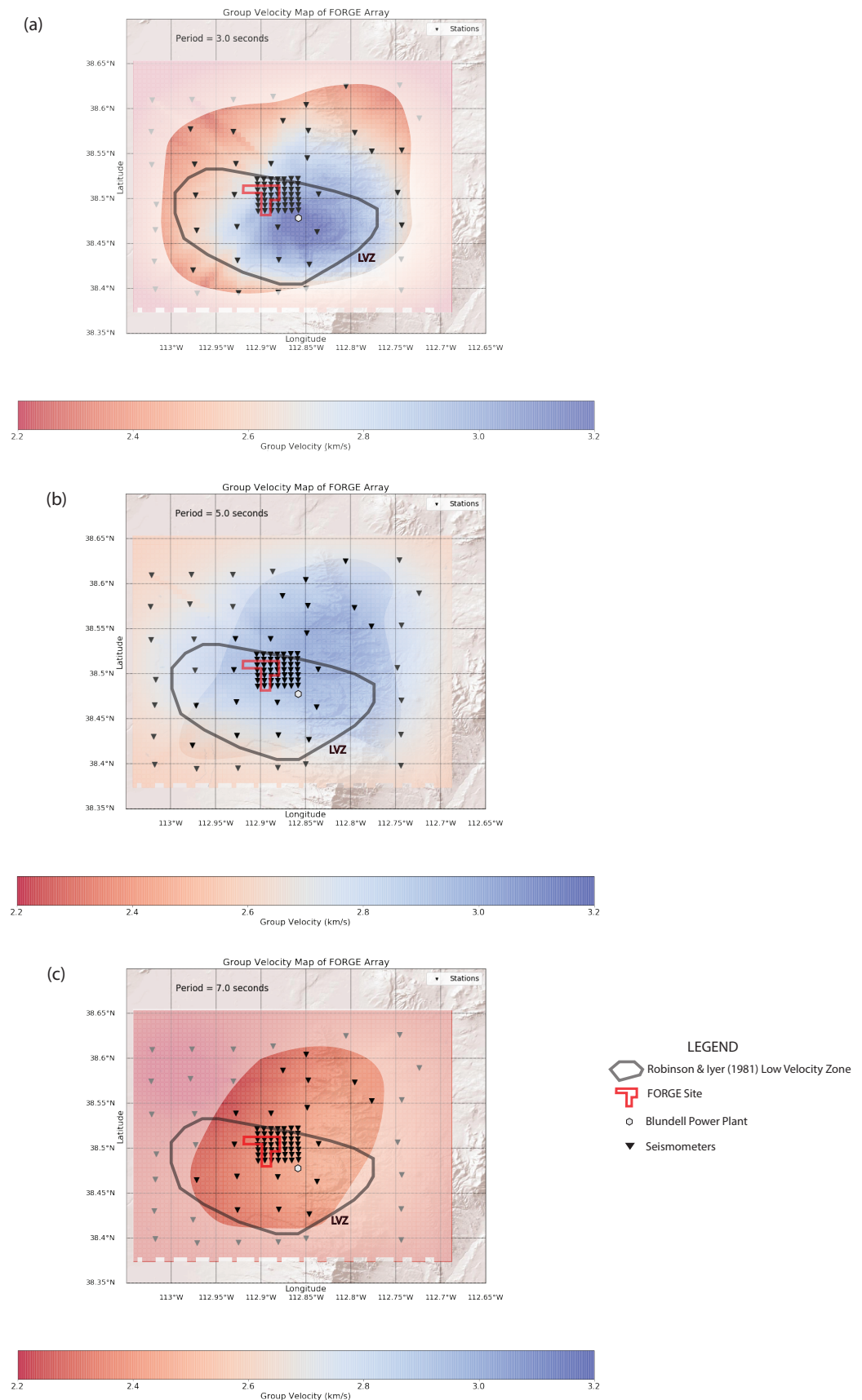


**Figure 11.** Tomographic models for the Mineral Mountains from the FORGE array. Group velocity maps are plotted in 0.001 degree grid cells. **(a)** Group velocity map for 3 second period, **(b)** group velocity map for 5 second period, **(c)** group velocity map for 7 second period. Low-velocity zone (LVZ) identified by Robinson and Iyer (1981) is outlined. Masked region represents the approximate area that has enough crossing ray paths to resolve structure. Qualitatively, this is the region with the most constrained results.

consistent with other shallow subsurface Vs30 studies in the area (Zhang and Pankow, 2018). We also note higher velocities towards the Mineral Mountains and interpret this to be a shallowing of the bedrock contact. Results from this study will form a baseline for future ambient noise studies that will be conducted in the region.

## DATA AND RESOURCES

Seismic data used in this experiment are currently available from a University of Utah data server on request; send inquiries to andyjtrow@gmail.com. Seismic data were processed using Seismic Analysis Code (Helffrich et al., 2013). We operate within the Python framework and rely on existing toolboxes and numerical and plotting libraries, namely NumPy, Matplotlib, Basemap, and ObsPy (Beyreuther et al., 2010).

## ACKNOWLEDGMENTS

We thank Jamie Farrell, Nathan Downey, Rick Allis and Stephanie Carney for thoughtful reviews of the manuscript.

## REFERENCES

- Allis, R., Gwynn, M., Hardwick, C., Kirby, S., Bowers, R., Moore, J.N., Wannamaker, P., and Simmons, S. 2017, Characteristics of the Cove Fort-Dog Valley-Twin Peaks thermal anomaly, Utah: Proceedings of the 42nd Workshop on Geothermal Reservoir Engineering, Stanford University, Stanford, California.
- Barker, C.A., 1986, Upper-crustal structure of the Milford Valley and Roosevelt Hot Springs, Utah region, by modeling of seismic refraction and reflection data: Salt Lake City, University of Utah, M.S. thesis, 101 p.
- Barmin, M.P., Ritzwoller, M.H., and Levshin, A.L., 2001, A fast and reliable method for surface wave tomography. *Pure and Applied Geophysics*, 158, 1351–1375.
- Bensen, G.D., Ritzwoller, M.H., Barmin, M.P., Levshin, A.L., Lin, F., Moschetti, M.P., Shapiro, N.M., and Yang, Y., 2007, Processing seismic ambient noise data to obtain reliable broad-band surface wave dispersion measurements, *Geophysical Journal International*, 169, 3, 1239–1260.
- Benz, H.M., Smith R.B., and Mooney W.D., 1990, Crustal structure of the Northwestern Basin and Range Province from the 1986 Program for Array Seismic Studies of the Continental Lithosphere Seismic Experiment, *Journal of Geophysical Research*, 95(B13), 21823–21842.
- Beyreuther, M., Barsch, R., Krischer, L., Megies, T., Behr, Y., and Wassermann, J., 2010, ObsPy: A Python Toolbox for Seismology. *Seismological Research Letters*, 81(3), 530–533.
- Bowden, D.C., Tsai, V.C., and Lin, F.C., 2015, Site amplification, attenuation, and scattering from noise correlation amplitudes across a dense array in Long Beach, CA, *Geophysical Research Letters*. 42, 1360–1367.
- Blackwell, D.D., 1983, Heat flow in the northern Basin and Range province, *in* The Role of Heat in the Development of Energy and Mineral Resources in the Northern Basin and Range Province, edited by Geothermal Resources Council, Spec. Rep., 13, 81–93.
- Calò, M., Kinnaert, X., and Dorbath, C., 2013, Procedure to construct three-dimensional models of geothermal areas using seismic noise cross-correlations: application to the Soultz-sous-Forêts enhanced geothermal site, *Geophysical Journal International*, 194, 3, 1893–1899.
- Edwards, M.C., and Chapman, D.S., 2013, Geothermal resource assessment of the Basin and Range province in western Utah report and heat flow map: unpublished report to the Utah Geological Survey, 121 p.121.
- Faulder, D.D., 1991, Conceptual geologic model and native state of the Roosevelt Hot Springs hydrothermal system. Proceedings of the 16th Workshop on Geothermal Reservoir Engineering, Stanford University, 1991. 131–142.
- Hansen, S.M., and Schmandt, B., 2015, Automated detection and location of microseismicity at Mount St. Helens with a large-N geophone array, *Geophysical Research Letters*. 42, 7390–7397.

- Hardwick C.L., Gwynn, M., Allis, R., Wannamaker, P., and Moore, J., 2016, Geophysical signatures of the Milford, Utah FORGE site: Proceedings, 41st Workshop on Geothermal Reservoir Engineering, Stanford University, Stanford, CA.
- Haubrich, R.A., Munk, W.H., and Snodgrass, F.E., 1963, Comparative spectra of microseisms and swell. *Bulletin of the Seismological Society of America*, 53 (1) (1963), 27–37.
- Helffrich, G., Wookey, J., and Bastow, I., 2013, *The Seismic Analysis Code: A Primer and User's Guide*. Cambridge: Cambridge University Press.
- Herrmann R.B., Benz H., and Ammon C.J., 2011, Monitoring the earthquake source process in North America, *Bulletin of the Seismological Society of America*, 101, 2609–2625.
- Lehujeur, M, Vergne, J., Maggi, and A., Schmittbuhl, J., 2017, Ambient noise tomography with non-uniform noise sources and low aperture networks: case study of deep geothermal reservoirs in northern Alsace, France, *Geophysical Journal International*, 208, 1, 193–210.
- Levshin, A.L., Yanovskaya, T.B., and Lander, AV., 1989, *Seismic Surface Waves in Laterally Inhomogeneous Earth*, Kluwer Acad., Norwell, Mass.
- Li, Z., Peng, Z., Hollis D., Zhu, L., and McClellan, J., 2018, High-resolution seismic event detection using local similarity for Large-N arrays, *Scientific Reports* 8:1646.
- Li, Z., Peng, Z., Meng, X., Inbal, A., Xie, Y., Hollis, D., and Ampuero, J.P., 2015, Matched Filter Detection of Microseismicity in Long Beach with a 5200-station Dense Array, SEG Technical Program Expanded Abstracts 2015, Society of Exploration Geophysicists, 2615–2619.
- Lin, F.-C., Moschetti, M.P., and Ritzwoller, M.H., 2008, Surface wave tomography of the western United States from ambient seismic noise: Rayleigh and Love wave phase velocity maps. *Geophysical Journal International*, 173, 281–298.
- Lin, F.-C., Li, D., Clayton, R.W., and Hollis, D., 2013, High-resolution 3D shallow crustal structure in Long Beach, California: Application of ambient noise tomography on a dense seismic array. *Geophysics*, 78(4), Q45–Q56.
- Moore J.N., and Nielson, D.L., 1994, An overview of the geology and geochemistry of the Roosevelt Hot Springs geothermal system, Utah: Utah Geological Association Publication 23, 25–36.
- Robinson, R., and Iyer, H.M., 1981, Delineation of a low-velocity body under the Roosevelt Hot Springs geothermal area, Utah, using teleseismic P-wave data, *Geophysics* 46(10), 1456–1466.
- Shapiro N.M., and Campillo, M., 2004, Emergence of broadband Rayleigh waves from correlations of the ambient seismic noise, *Geophysical Research Letters*, 31.
- Shapiro, N.M., Campillo, M., Stehly, L., and Ritzwoller, M.H., 2005, High-resolution surface-wave tomography from ambient seismic noise. *Science*, 307(5715), 1615–1618.
- Simmons, S., Moore, J., Allis, R., Kirby, S., Jones, C., Bartley, J., Kleber, E., Knudsen, T., Miller, J., Hardwick, C., Rahilly, K., Gwynn, M., McLennan, J., Forbes, B., Podgorney, R., Pankow, K., Wannamaker, P., and Fischer T., 2018, A revised geoscientific model for FORGE Utah EGS Laboratory, Proceedings, 43rd Workshop on Geothermal Reservoir Engineering, Stanford University, Stanford, CA.
- Simmons, S., Kirby, S., Jones, C., Moore, J., and Allis, R., 2016, The geology, geochemistry, and hydrology of the EGS FORGE site, Milford Utah: Proceedings, 41st Workshop on Geothermal Reservoir Engineering, Stanford University, 10 p.
- Smith, R.B., and Bruhn, R.L., 1984, Intraplate extensional tectonics of the Eastern basin-Range: Inferences on structural style from seismic reflection data, regional tectonics, and thermal-mechanical models of brittle-ductile deformation, *Journal of Geophysical Research*, 89(B7), 5733–5762.
- Snieder, R., 2004, Extracting the Green's function from the correlation of coda waves: A derivation based on stationary phase, *Physical Reviews E*, 69, 046610.
- Trow, A.J., Zhang, H., Record, A.S., Mendoza, K.A., Pankow, K.L., Wannamaker, P.E., 2018, Microseismic Event Detection Using Multiple Geophone Arrays in Southwestern Utah, *Seismological Research Letters*, 0895-0695.
- Wang, Y., Lin, F.-C., Schmandt, B., and Farrell, J., 2017, Ambient noise tomography across Mount St. Helens using a dense seismic array, *Journal of Geophysical Research, Solid Earth*, 122, 4492–4508.
- Ward, K.M., 2015, Ambient noise tomography across the southern Alaskan Cordillera. *Geophysical Research Letters*, 42(9), 3218–3227.

- Ward, K.M., and Lin, F.C., 2017, On the Viability of Using Autonomous Three- Component Nodal Geophones to Calculate Teleseismic Ps Receiver Functions with an Application to Old Faithful, Yellowstone, *Seismological Research Letters* 88(5), 1268–1278.
- Ward, S.H., Parry, W.T., Nash, W.P., Sill, W.R., Cook, K.L., Smith, R.B., and Bowman, J.R., 1978, A summary of geology, geochemistry, and geophysics of the Roosevelt Hot Springs thermal area, Utah, *Geophysics* 43(7), 1515–1542.
- Whidden, K.M., and Pankow, K.L., 2012, A catalog of regional moment tensors in Utah from 1998 to 2011, *Seismological Research Letters*, 83, 775–783.
- Wu, S.-M., Ward, K.M., Farrell, J., Lin, F.-C., Karplus, M., and Smith, R.B., 2017, Anatomy of Old Faithful From Subsurface Seismic Imaging of the Yellowstone Upper Geyser Basin, *Geophysical Research Letters*, 44, 10, 240–247.
- Yao, H., Beghein, C., and Van Der Hilst, R.D., 2008. Surface wave array tomography in SE Tibet from ambient seismic noise and two-station analysis—II. Crustal and upper-mantle structure, *Geophysical Journal International*, 173, 205–219.
- Zhang, H., and Pankow, K., 2018, A Bayesian Application of SPAC to Resolve Vs30 Using Nodal Seismic Instruments. *Seismology of the Americas Meeting*, May 14–17, 2018, Miami, FL.